ADVANCED MATERIALS
www.advmat.de

Control of Mechanical and Fracture Properties in Two-Phase Materials Reinforced by Continuous, Irregular Networks

Tommaso Magrini, Chelsea Fox, Adeline Wihardja, Athena Kolli, and Chiara Daraio**

Composites with high strength and high fracture resistance are desirable for structural and protective applications. Most composites, however, suffer from poor damage tolerance and are prone to unpredictable fractures. Understanding the behavior of materials with an irregular reinforcement phase offers fundamental guidelines for tailoring their performance. Here, the fracture nucleation and propagation in two phase composites, as a function of the topology of their irregular microstructures is studied. A stochastic algorithm is used to design the polymeric reinforcing network, achieving independent control of topology and geometry of the microstructure. By tuning the local connectivity of isodense tiles and their assembly into larger structures, the mechanical and fracture properties of the architected composites are tailored at the local and global scale. Finally, combining different reinforcing networks into a spatially determined meso-scale assembly, it is demonstrated how the spatial propagation of fracture in architected composite materials can be designed and controlled a priori.

1. Introduction

Composite materials offer many advantages over traditional materials, such as being lightweight while maintaining a high strength and stiffness,[1,2] but they suffer from lack of toughness and poor damage tolerance.[3–6] One way to improve their crack response is to tailor the reinforcing phase architecture.[7–10] Fiber reinforcements, for example, exploit crack bridging between fibers for toughening. Introducing fibers and other high-aspect-ratio reinforcing elements in the design of composite materials often leads to direction-dependent mechanical properties and anisotropic fracture resistance.[11] Depending on the reinforcing elements' alignment direction, composites can be either toughened by high fracture energy dissipative mechanisms, such as fiber bridging and fiber pullout, or be subject to delamination fractures, which occur at the fiber-matrix interface.[11–14] On the contrary, randomly distributed inclusions, which primarily toughen the material through microcracking and secondary crack formation, often lead to composite materials with isotropic fracture properties.[15–17] Developing materials that use multiple toughening mechanisms, like bridging, deflecting, or even arresting the propagation of cracks, has the potential to improve the amount of absorbed fracture energy. This was recently demonstrated in bioinspired architected composites, where the internal microstructure was finely tailored to control crack propagation behavior.[18,19] The combination of multiple toughening mechanisms can also be achieved by fabricating composite materials with irregular reinforcing networks.[20,21] Irregular microstructures are common in biological structural materials[22–25] and understanding their behavior during loading and fracture is relevant for the design of architected materials with tailored load-bearing performance. Irregular networks can control the fracture and toughening behavior of materials through the creation of meso-scale structures with different dimensions and orientations that cause multiple fracture nucleation and propagation events. Finally, reinforcing composites with irregular networks allows the creation of materials with direction-independent mechanical properties, a desirable feature in structural and load-bearing applications. Here, we describe how network coordination influences the global mechanical properties of two-phase materials, like strength, stiffness, and energy dissipated during fracture, as well as the role of local mechanisms on fracture nucleation and propagation. Introducing desired irregular networks as composite reinforcement and achieving a fine control over their assembly across multiple lengthscales, from the micro- to the centimeter-scale, requires advances in both numerical design and manufacturing. In recent work, machine-learning and data-driven approaches were used to computationally design hierarchical architected materials.[26] Here, we employ algorithms that "grow" regular and irregular networks[27] for composite design and use multimaterial additive manufacturing processes for fabrication.

2. Design of Irregular Reinforcement

To design the stiff reinforcement phase of our two-phase composites, we utilized a virtual growth algorithm (Supporting Information, Discussion 1), which tessellates a set of bimaterial tiles on a discretized spatial grid, following a set of connectivity rules.[27] We used a combination of 2-coordinated tiles ([L]

T. Magrini, C. Fox, A. Wihardja, A. Kolli, C. Daraio
Engineering and Applied Science
California Institute of Technology
Pasadena CA 91125, USA
E-mail: magrini@caltech.edu; daraio@caltech.edu

The ORCID identification number(s) for the author(s) of this article can be found under https://doi.org/10.1002/adma.202305198

DOI: 10.1002/adma.202305198

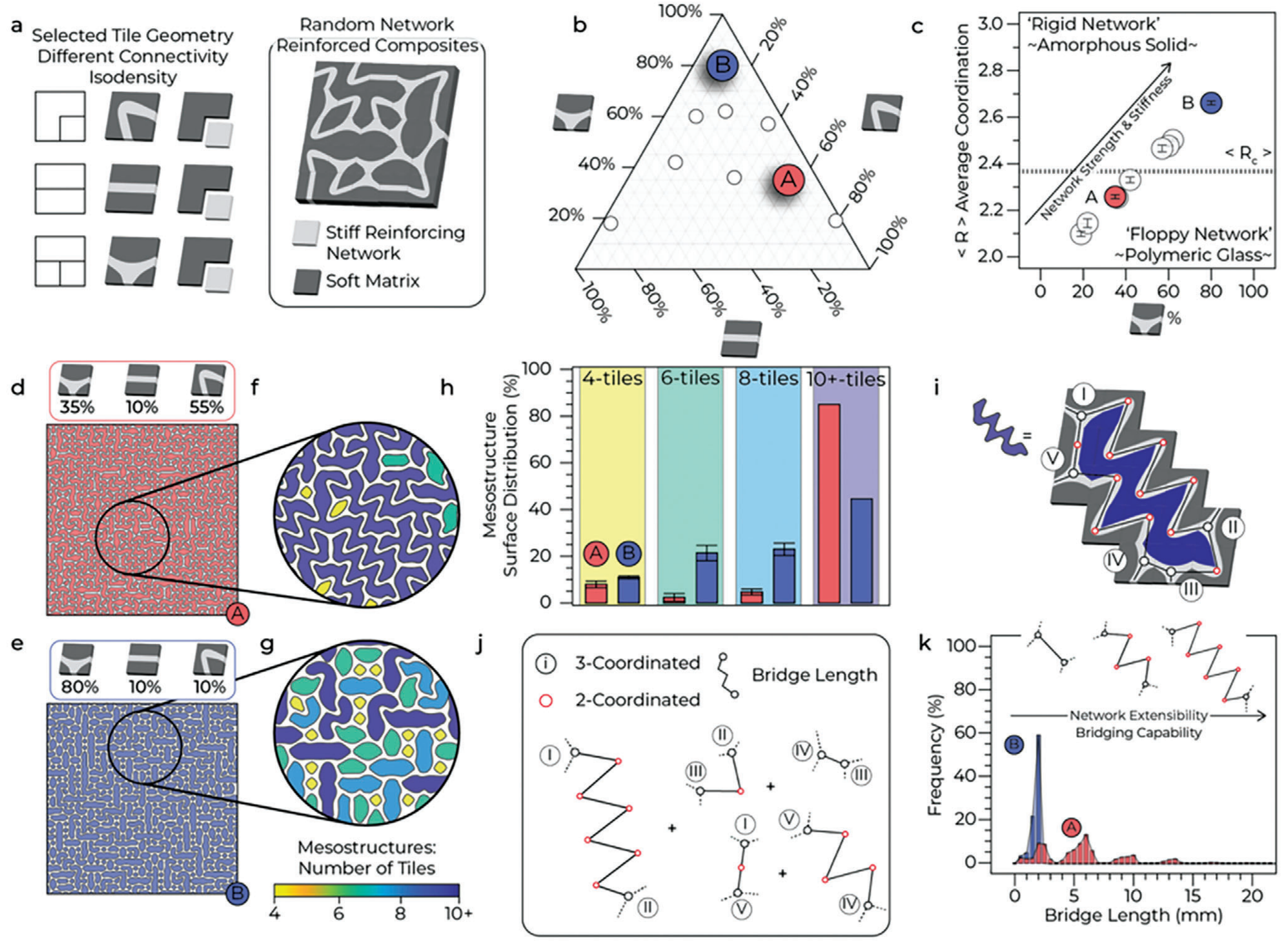

Figure 1. Architecture of two-phase materials. a) Selected isodensity tile geometries and composite assembly. b) Compositional design space in a ternary diagram. (A) and (B) architectures are represented by red and blue circles, respectively. c) Average coordination <*R*> as a function of [T] tiles content. (A) and (B) reinforcing networks are represented by red and blue circles, respectively. d,e) Representative (A) and (B) architectures (d and e, respectively). f g) Close-up view of meso-structures that populate (A) and (B) architectures in (d) and (e), respectively. Yellow, green, cyan, and blue represent 4, 6, 8, and 10+ tiles meso-structures, respectively. h) Meso-structure distributions in (A) (red bars) and (B) architectures (blue bars). i) Example of meso-structure with labeled coordination and bridges. j) Expanded version of (i). k) Comparison of bridge length and their frequency for (A) and (B) architectures (red and blue, respectively).

and [-]) and 3-coordinated tiles ([T]) and ensured that each tile had the same volume fraction of stiff reinforcing phase and soft matrix phase (**Figure 1**a, left). We combined these tiles to generate composites with a stiff reinforcing irregular network (white) and a soft elastomeric matrix (black) (Figure 1a, right). The virtual growth algorithm ensures continuity between the two phases through modifiable connectivity rules (Figure S1, Supporting Information). Depending on the relative composition of 2- and 3-coordinated tiles, the virtual growth algorithm creates various composites with the same volume fraction of reinforcement, but a large ternary design space (Figure 1b). We expect the shape and directional tile connectivity to influence the local deformation mechanisms accessible within the clusters, with [L] shaped tiles showing bending-dominated local deformations and straight [-] tiles showing stretching-dominated behaviors.

3. Network Characterization

We evaluate the properties of the reinforcing networks using frameworks developed to describe covalent random networks (Supporting Information Discussion 2), at two hierarchical scales. At the global scale, we evaluate the average coordination of the materials at constant density, and at the local scale, we analyze how growth rules affect the formation of characteristic meso-structures. We evaluate the average coordination <*R*> in the reinforcing networks, accounting for the presence of dangling bonds, unconnected ligaments at the network edges (Figure 1c).[28,29] Scaling linearly with the volume fraction of 3-coordinated tiles, we expect <*R*> to influence the global mechanical properties, like strength and stiffness, as reported in other amorphous material systems.[30–32] To understand the effect of the reinforcing network architecture on the composite properties, we compare two different compositions with significantly different average coordination: (A)-networks (35 [T], 10 [-], 55 [L]), dominated by 2-coordinated tiles and floppy modes; and (B)-networks (80 [T], 10 [-], 10 [L]), dominated by 3-coordinated tiles and that are purely rigid (Figure 1b,c, red and blue circles, respectively).

Despite having the same reinforcing and matrix phase volume fractions, (A)- and (B)-network reinforced composites (NRC's) form different local meso-structures, defined as the matrix domains enclosed by reinforcing network (Figure 1d,e). While the average coordination of the reinforcing network explains the global mechanical behavior of the materials, studying the meso-structures that pattern each composite is key to understand their local properties. First, the meso-structures are categorized and mapped based on size and number of constitutive tiles (Figure 1f,g). Then, their surface distribution is used to indicate the texture of (A)- and (B)-NRC's (Figure 1h). Additionally, the number density of each meso-structure (Figure S2, Supporting Information), their angle of orientation (Figure S3, Supporting Information), and the effect that small meso-structures have on their surroundings (Figure S4, Supporting Information) are important descriptors of these architected composites.

We characterize the reinforcing networks by drawing parallels with the concept of network bridges, often used in studying of the mechanical performance of covalent random networks.[28,29] A bridge (black solid lines, Figure 1i,j) connects two 3-coordinated tiles, considered anchored in the network (I–V white circles, Figure 1i,j). It was demonstrated that a bridge composed of six or more 2-coordinated tiles (red circles, Figure 1i,j) forms a floppy region within the network.[28,29] The presence of floppy domains in a stiff, yet deformable, reinforcing network influences the local mechanical composite performance, resulting in a globally more extensible and deformable material (Figure S5, Supporting Information). In this context, the presence of an incompressible matrix phase is important to prevent large bridge deformations. Because of the different content of 3-coordinated tiles, (A)-NRC's display a multimodal distribution of bridge lengths, which are significantly longer than those of (B)-NRC's (Figure 1k).

4. Mechanical Properties

Although (A)- and (B)-NRC's have the same volume fraction of reinforcement and matrix phases, the difference in average coordination, bridge length and different meso-structure populations influence the mechanical properties at both global and local scales. To measure experimentally the mechanical properties of the chosen architectures, we additively manufactured composite samples using a polyjet printer (Stratasys Objet500 Connex3). Recent studies have focused on experimentally determining the mechanical and physical properties of objects printed by polyjet printing and shed light on the relationship between the printing parameters and the final performance of the part.[33–35] In our study, a stiff viscoelastic resin (VeroWhite Polyjet Resin) and a soft elastomeric resin (TangoBlack Polyjet Resin) were chosen for the reinforcing phase and matrix phase, respectively. Both resins are commercially available, and their constitutive properties fall within ranges reported in literature (Figure S7, Supporting Information).[18,36–38] We combined these two materials in a polymer composite with a volume fraction of reinforcing phase of 0.3. At this volume fraction, we observed that the composites display a desired tradeoff between rigidity and extensibility (Figure S8, Supporting Information), while the reinforcing network thickness is one order of magnitude larger than the polyjet printer resolution limit (Figure S9, Supporting Information). To characterize their mechanical response, we performed plate tension experiments and confirmed that at the global scale, the purely rigid-like (B)-NRC's achieve higher strength and higher stiffness than the (A)-NRC's (**Figure 2**a,b).

Despite a significant difference in the global mechanical properties, the composites display similarities in the local scale mechanisms that determine the initiation and propagation of fractures. Due to the remarkable adhesion properties between the two resins used in this study,[39] fracture initiation does not occur at the interface between the matrix and the reinforcing network, in either pristine or pre-notched samples, but within the matrix (Figure S7, Supporting Information). Void nucleation in the matrix phase initiates the composite fracture process, similar to the ductile fracture of metals.[40] Void formation is followed by matrix detachment from the reinforcing network, resulting in steady void growth (Figure 2c,d, I to III, respectively). In this propagation phase, the void growth and coalescence are hindered by the reinforcing network bridges, which elongate as the sample undergoes tensile loading. Thus, the average bridge length and extensibility before rupture become paramount, as these characteristics predict the strain of the reinforcing network before failure (Supporting Information Discussion 3). After the sequential failure of the bridges (Figure 2a,b, red and blue arrows, respectively), we observe the complete loss of composite integrity.

The local composite architecture becomes key during failure, as strain localization in selected meso-structures leads to fracture nucleation and growth, as confirmed by 2D Digital Image Correlation (DIC) at small strains (Figure 2e,f). Therefore, to design composites capable of dissipating the most fracture energy, one must act on both the global and local scale, tailoring the network rigidity and generating local meso-structures, to avoid localized strain fields. To achieve this, we modify the connectivity rules of the growth algorithm.

We changed the connectivity rules of the growth algorithm to increase energy dissipation during fracture in composites. By amending four tile connectivity rules (**Figure 3**a, top; Supporting Information Discussion 4, Figure S10, Supporting Information), we prevented the formation of large floppy domains, which increased network rigidity, stiffness, and strength. The modified networks displayed a purely rigid-like behavior, as shown by their higher average coordination than the original networks (Figure 3a, bottom). We tested the effect of the modified reinforcing networks on the composites' mechanical performance and fracture energy dissipation through plate tension experiments. As a result of their higher coordination, modified-(A)-network reinforced composites (Mod-(A)-NRC's) displayed higher ultimate tensile strength (UTS) and up to 60% increase in tensile stiffness (Figure 3b red and gray solid lines, respectively), while modified-(B)-network reinforced composites (Mod-(B)-NRC's) had a 5% reduction in stiffness as a result of the slightly lower average coordination (Figure 3e blue and gray solid lines, respectively). Although each composite begins failure at ≈10% tensile strain, the modified designs' damage tolerance dramatically improved. At high tensile strain (up to ≈16%), the Mod-NRC's carry a load of

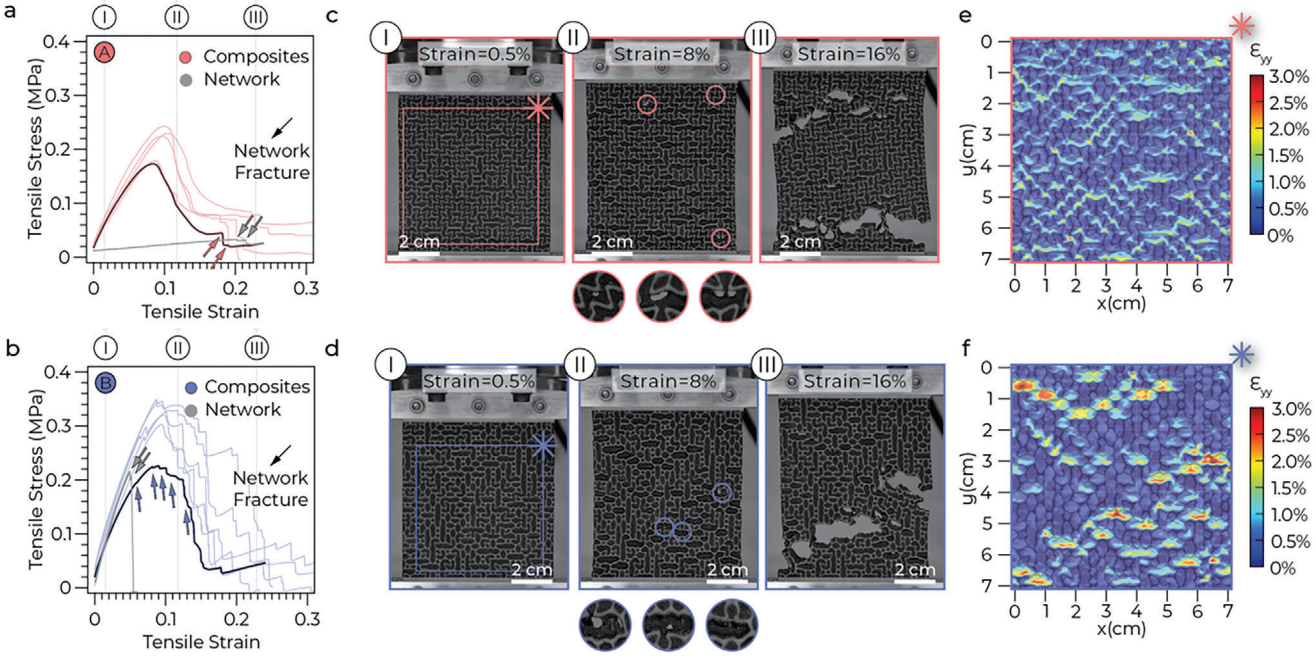

Figure 2. Mechanical characterization of composites. a,b) Engineering stress–strain curves recorded during uniaxial tension tests on plate geometries of (A)-NRC's and (B)-NRC's (red solid lines in a, blue solid lines in b, respectively). The solid black lines in (a,b) represent the response of samples photographed in (c,d), respectively. The solid gray lines in (a,b) represent the response of the same (A)-NRC and (B)-NRC samples, without the matrix phase. Fracture events in the reinforcing phase of (A)-NRC's and (B)-NRC's are indicated by red and blue arrows in (a) and (b), respectively, and in the reinforcing networks by gray arrows (see also Figure S6, Supporting Information). c,d) Fracture evolution in representative samples of (A)-NRC and (B)-NRC, respectively. The circles indicate the locations within the samples that display the signs of voids growth (circles in (c) and (d), frame II and insets in (c) and (d), frame II, bottom). e,f) Digital image correlation (DIC) maps of the representative samples of (A)-NRC and (B)-NRC recorded at 0.5% strain (e and f, respectively). The DIC maps refer to the areas of samples highlighted by (*) in frame I of c) and d).

≈70–80% their UTS (Figure 3c,d,f,g). As a comparison, their original counterparts at the same tensile strain had completely lost any load carrying capabilities, due to presence of sample-scale cracks and coalesced voids, resulting from the extensive failure of the reinforcing phase. Conventional calculations of the stress intensity factor and local stress concentration field require making assumptions based on continuum mechanics: for composite materials, the reinforcing feature sizes must be small compared to the size of the singularity zone, and the nonlinear damage must be confined to a small region within the singularity zone.[40] In our irregular composites, these conditions are not satisfied; meso-structures sizes are in the order of several mm (Figure S2, Supporting Information) and crack nucleation occurs in multiple locations within the microstructure (Figures 2c,d and 3d,g). In the present study, to highlight how these simple modifications to the reinforcing networks influence significantly the energy dissipated during fracture, we measured the modulus of toughness (MOT), taken as the area under the stress–strain curve. Modifying the reinforcing networks in (A) and (B) composites improved the total dissipated energy during fracture of up to ≈130% and ≈60%, respectively (Figure 3b,e, top).

Considering only global scale descriptors, like the average reinforcing network coordination, is insufficient to explain the higher strength of Mod-(B)-NRC's compared to (B)-NRC's. Thus, we evaluated the modified designs at the local scale, to investigate the effect that simple modifications of the connectivity rules had on the meso-structures. First, we notice by visual inspection that the modified composites (Figure 3h,i, bottom) have a significantly different internal structure than their original counterparts (Figure 3h,i, top). The modified architectures feature a more homogeneous distribution of meso-structures, which are quantified through the polydispersity index (PDI) (Figure 3h,i; and Supporting Information Discussion 5). The decrease in PDI by 33% for (A)-NRC's and by 20% for (B)-NRC's, confirms that more stringent connectivity rules homogenize and coarsen the meso-structures sizes (Figure S11, Supporting Information). Furthermore, the modified composites feature meso-structures that display a more homogeneous angle of orientation with respect to their original counterparts (Figure 3j,k). As a result of the more homogeneous size and orientation distribution of domains, the modified composites are subject to a more homogeneous distribution of the deformation during loading, preventing high strain localization (Figure S12, Supporting Information) and leading to the multiple uniformly distributed void nucleation sites in the matrix (Figure 3d,g). Finally, we evaluated the effect of the modifications on bridges length distributions. In Mod-(A)-NRC's, the increase in short bridges confirms that the newly generated networks are more constrained and thus rigid, compared to their original counterparts (Figure 3l). Conversely, Mod-(B)-networks have a distribution of bridge lengths that shifts toward larger sizes and becomes multimodal, becoming like those of (A)-networks, suggesting the generation of reinforcing networks with higher local extensibility and hence, higher bridging capability (Figure 3m).

ADVANCED MATERIALS
www.advmat.de

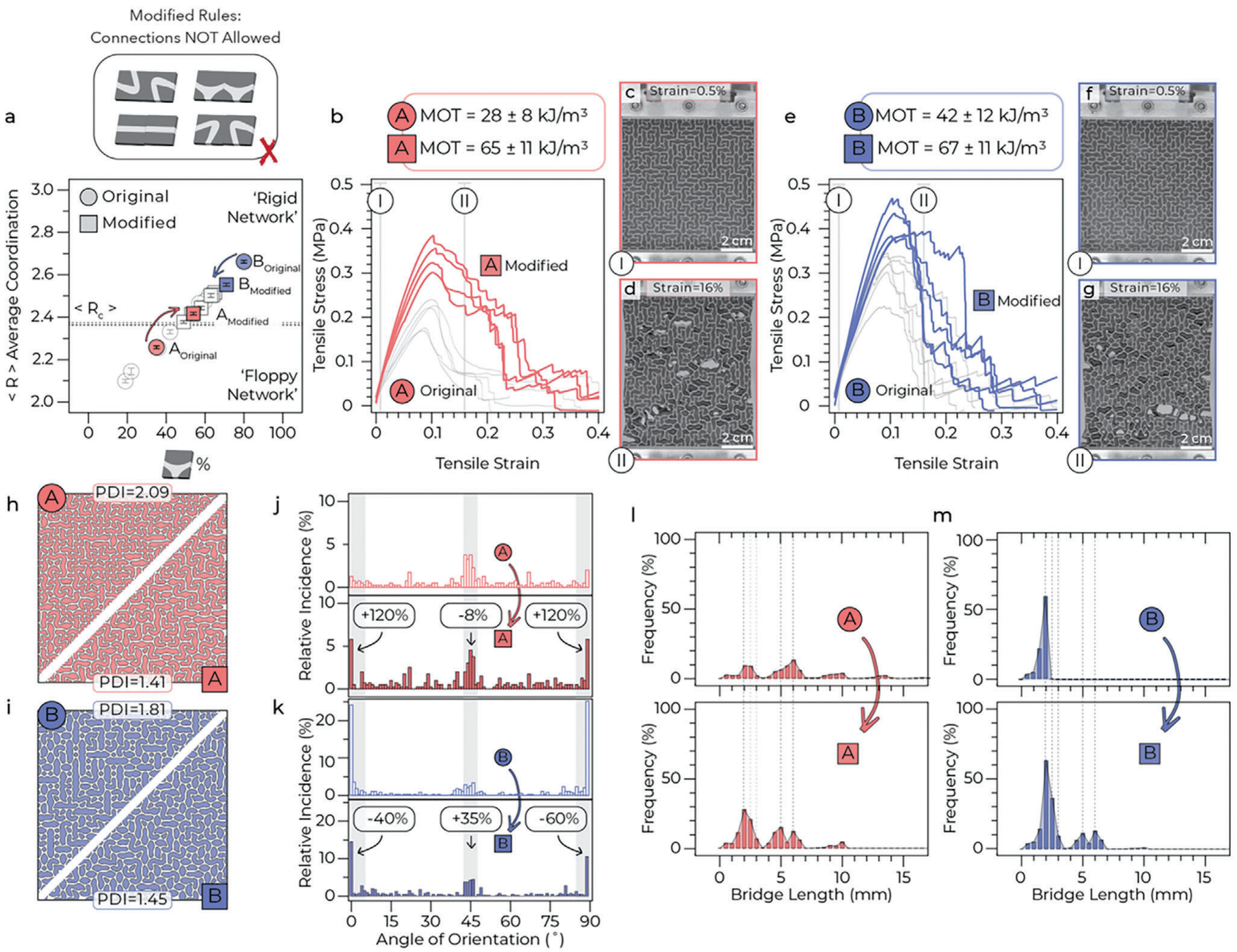

Figure 3. Modified composites and their performance. a) Modifications of connectivity rules and average coordination number as a function of [T] tiles (top and bottom, respectively). b) Engineering stress–strain diagram of Mod-(A)-NRC's (red solid lines) and of original (A)-NRC's (gray solid lines). The modulus of toughness (MOT) is reported for both composites at the top of the diagram. c,d) Fracture evolution in representative Mod-(A)-NRC at 0.5% and 16% strain (c and d, respectively). e) Engineering stress–strain diagram of Mod-(B)-NRC's (blue solid lines) and of the original (B)-NRC's (gray solid lines). The MOT is reported for both composites at the top of the diagram. f,g) Fracture evolution in representative Mod-(B)-NRC at 0.5% and 16% strain (f and g, respectively). h,i) Modification of microstructure of (A)- and (B)-networks (h and i, respectively) and measured polydispersity index (PDI) for each network. j,k) Variation in relative meso-structure orientation distribution of (A) and (B)-networks (j and k, respectively). l) Frequency of bridge lengths for (A)- and Mod-(A)-networks (top and bottom, respectively). m) Frequency of bridge lengths for (B)- and Mod-(B)-networks (top and bottom, respectively).

We developed a method to control crack trajectory in network reinforced composites by creating hierarchical microstructures that combine local rules, meso-scale assemblies, and macroscale connectivity networks at a constant density. We drew inspiration from biological composites like mother-of-pearl[41–45] and cortical bone,[46–48] which deflect incoming cracks and dissipate fracture energy. Our meso-scale assemblies feature rational designs of "strong and tough" network portions combined with "soft" network portions. We created two laminate configurations with complementary meso-scale arrangements (**Figure 4**a I and b I, respectively) and found that the (A)-NRC's domains carry most of the strain regardless of their spatial arrangement. For an applied 0.5% strain, (A)-NRC's domains are subject to ~0.8% strain whereas Mod-(B)-NRC's domains experience as little as 0.3% strain (Figure 4c,d). We can thus control the fracture trajectory through domain assembly, since fracture nucleates (Figure 4a II,b II) and propagates (Figure 4a III,b III) in "soft" domains. These properties are also consistent with crack propagation observed in single edge notch tension tests (SENT) (Figure S7). We take inspiration from the cross section of cortical bone, composed of tightly packed osteons enveloped by the cement lines, specifically designed to arrest and guide incoming cracks on tortuous trajectories (Figure 4e).[49–51] In our cortical bone-inspired assembly, we embedded strong and tough osteon-inspired high coordination domains in a floppy and low coordination matrix domain (Figure 4f). At 7% strain, it is already visible how the strain localizes in the floppy portions of the composite (Figure 4g), leading to fracture nucleation in the central matrix area (left side,

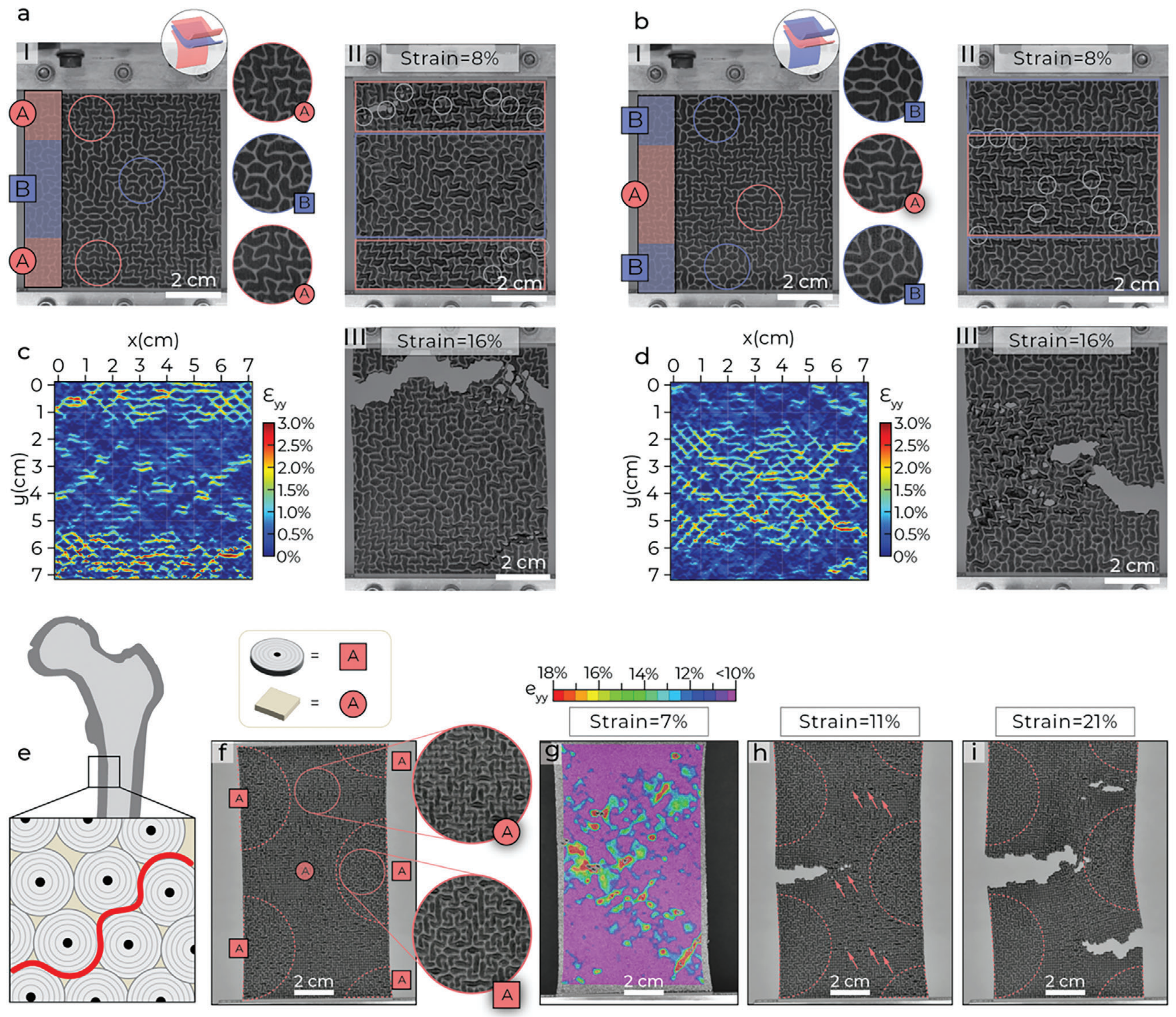

Figure 4. Multiarchitecture meso-scale assemblies. a,b) Laminate assemblies: (A), Mod-(B), (A) and Mod-(B), (A), Mod-(B) (a and b, respectively). The insets highlight differences in reinforcing architecture. Fracture evolution (I, II, III (a) and (b), respectively). c,d) DIC maps at 0.5% strain in laminate assemblies. e) Sketch of cross section of cortical bone f) Cortical bone inspired meso-scale assembly. Mod-(A) constitutes osteon-inspired features (dashed red semicircles), (A) constitutes the matrix phase. g) DIC map at 7% strain and highlighting strain distribution in cortical bone inspired assembly. h,i) Fracture evolution at 11% and 21% strain (h and i, respectively).

Figure 4h), that is then arrested as it approaches the opposite osteon-domain (right side, Figure 4h). Meanwhile, crack nucleation above and below the plane of propagation initiates the desired process of renucleation and redirection of the fracture, critical to deflect its trajectory (red arrows, Figure 4h) and to successfully shield the osteon domains (Figure 4i).

5. Conclusions

In this study, we developed architected composite materials that exhibit a high degree of hierarchical order through material design. By utilizing a virtual growth algorithm, we manipulated the local connectivity between isodensity tiles, resulting in the formation of larger meso-structures, which were merged to create sample-sized assemblies with predetermined spatial arrangements. This approach enabled tailoring the mechanical and fracture properties of the architected composites, at the local and global scales. We envision that the use of different sets of starting tiles and the combination of different reinforcing and matrix phases, will allow for fine-tuning the activation of desired reinforcement and fracture energy dissipation mechanisms. Building on our proof-of-concept observations, we hypothesize that controlling the spatial arrangement and continuity between the soft and stiff phases can be used to prevent interfacial failure, while their intentional design can facilitate the precise spatial distribution of fractures in architected composites.

Supporting Information

Supporting Information is available from the Wiley Online Library or from the author.

Acknowledgements

The authors thank P. Arakelian, K. Liu, T. Zhou, C. McMahan, and J. Boddapati for the fruitful discussions. The authors acknowledge MURI ARO W911NF-21-S-0008 for the financial support. T.M. acknowledges the Swiss National Science Foundation for the financial support (SNSF Post-doc.Mobility Fellowship, P500PT_203197/1).

Conflict of Interest

The authors declare no conflict of interest.

Data Availability Statement

The data that support the findings of this study are available from the corresponding author upon reasonable request.

Keywords

Additive manufacturing, Composite Materials, Irregular Materials, Mechanics of materials

Received: May 31, 2023
Revised: September 5, 2023
Published online:

[1] R. F. Gibson, *Compos. Struct.* **2010**, *92*, 2793.
[2] J. Fan, J. Njuguna, *Lightweight Composite Structures in Transport*, Elsevier, the Netherlands **2016**, pp. 3–34.
[3] B. Budiansky, J. W. Hutchinson, A. G. Evans, *J. Mech. Phys. Solids* **1986**, *34*, 167.
[4] A. G. Atkins, *Nature* **1974**, *252*, 116.
[5] F. M. Monticeli, F. R. Fuga, M. V. Donadon, *Thin-Walled Struct.* **2023**, *187*, 110742.
[6] R. O. Ritchie, *Nat. Mater.* **2011**, *10*, 817.
[7] M. Maurizi, B. W. Edwards, C. Gao, J. R. Greer, F. Berto, *Extreme Mech. Lett.* **2022**, *56*, 1.
[8] K. Wu, Z. Song, S. Zhang, Y. Ni, S. Cai, X. Gong, L. He, S.-H. Yu, *Proc. Natl. Acad. Sci. USA* **2020**, *117*, 15465.
[9] K. M. Conway, C. Kunka, B. C. White, G. J. Pataky, B. L. Boyce, *Mater. Des.* **2021**, *205*, 1.
[10] M. Sistaninia, R. Kasberger, O. Kolednik, *Compos. Struct.* **2018**, *185*, 113.
[11] L. K. Jain, R. C. Wetherhold, *Acta Metall. Mater.* **1992**, *40*, 1135.
[12] D. A. Norman, R. E. Robertson, *J. Appl. Polym. Sci.* **2003**, *90*, pp. 2740.
[13] A. C. Garg, *Eng. Fract. Mech.* **1988**, *29*, 127.
[14] J. P. Lucas, *Eng. Fract. Mech.* **1992**, *42*, 543.
[15] Y. Mao, J. W. Coenen, J. Riesch, S. Sistla, J. Almanstötter, J. Reiser, A. Terra, C. Chen, Y. Wu, L. Raumann, T. Höschen, H. Gietl, R. Neu, C. Linsmeier, C. Broeckmann, *Nucl. Fusion* **2019**, *59*, 086034.
[16] S. K. Gaggar, L. J. Broutman, *Am. Chem. Soc., Div. Org. Coatings Plast. Chem.* **1974**, *34*, 354.
[17] G. C. Jacob, J. M. Starbuck, J. F. Fellers, S. Simunovic, R. G. Boeman, *J. Appl. Polym. Sci.* **2006**, *100*, 695.
[18] Z. Jia, L. Wang, *Acta Mater.* **2019**, *173*, 61.
[19] L. S. Dimas, G. H. Bratzel, I. Eylon, M. J. Buehler, *Adv. Funct. Mater.* **2013**, *23*, 4629.
[20] T. F. W. Van Nuland, J. A. W. Van Dommelen, M. G. D. Geers, *Comput. Mater. Sci.* **2021**, *186*, 109947.
[21] Z. Hooshmand-Ahoor, M. G. Tarantino, K. Danas, *Mech. Mater.* **2022**, *173*, 104432.
[22] R. A. Metzler, F. Barthelat, J. J. Wilker, **2019**, *29*, 1805734.
[23] K. Robson Brown, D. Bacheva, R. S. Trask, *J. R. Soc. Interfaces* **2019**, *16*, 20180965.
[24] M. Jentzsch, M. C. Badstöber, F. Umlas, T. Speck, *Front. Mater.* **2022**, *9* https://doi.org/10.3389/FMATS.2022.979151/FULL.
[25] W. J. Whitehouse, *J. Microsc.* **1974**, *101*, 153.
[26] M. J. Buehler, **2023** https://doi.org/10.1088/1361-651X/accfb5.
[27] K. Liu, R. Sun, C. Daraio, *Science* **2022**.
[28] M. F. Thorpe, *J. Non Cryst. Solids* **1983**, *57*, 355.
[29] M. F. Thorpe, D. J. Jacobs, N. V. Chubynsky, A. J. Rader, *Rigidity Theory and Applications*, IOS Press, Amsterdam **1999**, p. 239.
[30] H. Tong, S. Sengupta, H. Tanaka, *Nat. Commun.* **2020**, *11*, 4863.
[31] F. Fan, S. Huang, H. Yang, M. Raju, D. Datta, V. B. Shenoy, A. C. T. Van Duin, S. Zhang, T. Zhu, *Modelling Simul. Mater. Sci. Eng.* **2013**, *21*, 074002.
[32] C. Meade, R. Jeanloz, *Science* **1988**, *241*, 1072.
[33] J. Mueller, K. Shea, C. Daraio, *Mater. Des.* **2015**, *86*, 902.
[34] L. J. Tan, W. Zhu, K. Zhou, *Adv. Funct. Mater.* **2020**, *30*, 2003062.
[35] A. Pilipovic, P. Raos, M. Sercer, *Int. J. Adv. Manuf. Technol.* **2009**, *40*, 105.
[36] J. Ryan, C. Dizon, A. H. Espera, Q. Chen, R. C. Advincula, *Addit. Manuf.* **2018**, *20*, 44.
[37] D. Bell, T. Siegmund, *Addit. Manuf.* **2018**, *21*, 658.
[38] V. Slesarenko, S. Rudykh, *Int. J. Eng. Sci.* **2018**, *123*, 62.
[39] R. J. Nash, Y. Li, *Eng. Fract. Mech.* **2021**, *253*, 107912.
[40] T. L. Anderson, *Fracture Mechanics: Fundamentals and Applications*, 3rd ed., CRC Press, Boca Raton, FL **2005**.
[41] T. Magrini, F. Bouville, A. R. Studart, *Open Ceram.* **2021**, *6*, 100109.
[42] F. Barthelat, H. Tang, P. Zavattieri, C. Li, H. Espinosa, *J. Mech. Phys. Solids* **2007**, *55*, 306.
[43] F. Barthelat, *Bioinspir. Biomim.* **2010**, *5*, 035001.
[44] J. W. Pro, F. Barthelat, *MRS Bull.* **2019**, *44*, 46.
[45] F. Barthelat, Z. Yin, M. J. Buehler, *Nat. Rev. Mater.* **2016**, *1*, 16007.
[46] R. O. Ritchie, *Philos. Trans. R. Soc., A* **2021**, *379*, 20200437.
[47] E. A. Zimmermann, B. Busse, R. O. Ritchie, *BoneKEy Rep.* **2015**, *4*, 743.
[48] K. J. Koester, J. W. Ager, R. O. Ritchie, *Nat. Mater.* **2008**, *7*, 672.
[49] T. Magrini, R. Libanori, A. Kan, A. R. Studart, *Rev. Bras. Ensino Fis.* **2021**, *43*, 1.
[50] R. B. Cook, P. Zioupos, *J. Biomech.* **2009**, *42*, 2054.
[51] R. Rabiei, S. Bekah, F. Barthelat, *Acta Biomater.* **2010**, *6*, 4081.